

Quantum-centric simulation of hydrogen abstraction by sample-based quantum diagonalization and entanglement forging

Tyler Smith,¹ Tanvi P. Gujarati,² Mario Motta,³ Ben Link,¹ Ieva Liepuoniute,² Triet Friedhoff,³ Hiromichi Nishimura,¹ Nam Nguyen,¹ Kristen S. Williams,¹ Javier Robledo Moreno,³ Caleb Johnson,³ Kevin J. Sung,³ Abdullah Ash Saki,³ Marna Kagele¹

¹*Integrated Vehicle Systems, Applied Mathematics,
Boeing Research & Technology, Huntington Beach, CA 92647, USA*

²*IBM Quantum, IBM Almaden Research Center, San Jose, CA 95120, USA*

³*IBM Quantum, IBM T. J. Watson Research Center, Yorktown Heights, NY 10598, USA*

The simulation of electronic systems is an anticipated application for quantum-centric computers, i.e. heterogeneous architectures where classical and quantum processing units operate in concert. An important application is the computation of radical chain reactions, including those responsible for the photodegradation of composite materials used in aerospace engineering. Here, we compute the activation energy and reaction energy for hydrogen abstraction from 2,2-diphenyldipropene, used as a minimal model for a step in a radical chain reaction. Calculations are performed using a superconducting quantum processor of the IBM Heron family and classical computing resources. To this end, we combine a qubit-reduction technique called entanglement forging (EF) with sample-based quantum diagonalization (SQD), a method that projects the Schrödinger equation into a subspace of configurations sampled from a quantum device. In conventional quantum simulations, a qubit represents a spin-orbital. In contrast, EF maps a qubit to a spatial orbital, reducing the required number of qubits by half. We provide a complete derivation and a detailed description of the combined EF and SQD approach, and we assess its accuracy across active spaces of varying sizes.

I. INTRODUCTION

Free radicals, because of their high reactivity, can be valuable chemical tools and harmful contaminants. Their rich chemical activity stems in part from their tendency to participate in chain reactions. Such reactions initiate with the formation of radicals from stable species, often through a homolytic bond cleavage triggered by exposure to heat or ultraviolet-visible (UV-vis) light. In a subsequent propagation phase, radicals react with stable molecules to form new radicals, e.g. through hydrogen abstraction. The reaction ends with the formation of a stable non-radical product from a reaction between radicals.

Radical chain reactions, and hydrogen abstraction in particular, are major pathways for photo-degradation of composite materials. In this context, they lead to phenomena like chain scission, polymer cross-linking and formation of oxidative products, that ultimately cause alterations in mechanical properties, discoloration, brittleness, and loss of performance. Composite materials used in aerospace-related applications typically consist of a polymer matrix reinforced with carbon or glass fibers, and they are used in the fabrication of aircraft fuselages and wings in lieu of metals due to high strength to weight ratio and corrosion resistance [1]. Photo-degradation of composite materials employed on in-service aircraft is a substantial issue for airplane manufacturers, leading to hundreds of millions of dollars in maintenance and repair costs. For example, the photo-oxidation of the epoxy resin used in aircraft wings results in the peeling of the

overlying primer and topcoat paint layers, see Fig. 1, causing structural damage and surface blemishes [2].

Studies of this degradation process to date have involved experimental setups to mimic the effects of sunlight damage to composites with paint coatings [3]. Using such setups, research scientists within Boeing Research & Technologies' Chemical Technologies organization were able to reproduce the damage seen for in-service aircraft in days (while degradation of actual in-service aircraft composites occurs over multiple years) [4–6]. Experiments leveraging accelerated degradation showed that

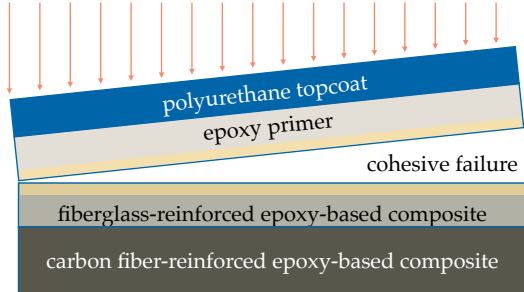


FIG. 1: Schematic illustration of the cohesive failure of a composite resin on commercial aircraft due to photo-degradation. While the topcoat and primer layers of paint provide some protection from incident light, after years of exposure enough ultraviolet and visible radiation penetrates through to the composite, ultimately leading to degradation.

the addition of a black paint coating between the white top coat and primer offers significant protection from resin degradation and the paint peeling it generates [7]. While this is a convenient palliative measure, a permanent and robust solution will require entirely new material formulations [8, 9]. More generally, materials selection for aerospace-related applications is typically performed through testing coupled with engineering judgment [10, 11]. Qualification of new materials is based on a combination of extensive testing, on-aircraft demonstration or empirical modeling of service life, without necessarily examining the detailed chemistry and physics underlying degradation effects [12, 13].

While experimental studies of composite degradation are well-established, ab initio models of epoxy resin degradation have yet to be developed, with current computational models relying on experiment for the determination of many critical parameters [14–16]. Few predictive tools are available for simulating material-environment interactions due to the complex nature of such interactions and the range of length scales involved [17]: aerospace parts are designed at scales ranging from centimeters to several meters, while the degradation mechanisms that lead to part failure in harsh environments – e.g., corrosion [18], high-temperature oxidation [19], ultraviolet degradation [20] – occur over only a few nanometers [21]. Modeling the mechanisms of polymer degradation from first principles would offer avenues towards predictive characterization for rational, rapid material designs. First-principles simulations may allow the study of reaction pathways for polymer degradation, leading to a deeper understanding of how chain scission, cross-linking, and other forms of degradation unfold [22], and ultimately aid in the design of future resins that incorporate stabilizers or other additives to mitigate the effects of ultraviolet and visible light [23].

Quantum-centric supercomputing (QCSC) [24] is an innovative computational paradigm, in which a quantum computer operates in concert with classical high-performance computing (HPC) resources. Classical pre-, peri-, and post-processing allows the introduction of quantum subroutines in the economy of classical HPC algorithms, and effectively distributes the computational cost of solution between classical and quantum processors. The QCSC architecture can significantly extend the domain of applicability of quantum computers through its use in algorithms with carefully designed quantum subroutines, as exemplified by the sample-based quantum diagonalization (SQD) method [25–29]. SQD uses a quantum device to sample electronic configurations. It uses HPC to correct for decoherence-induced breaking of molecular symmetries [26] as well as to solve the Schrödinger equation in a subspace defined by sampled and processed configurations.

In this work, we simulate hydrogen abstraction by a free radical with SQD, and to this end we introduce two methodological extensions. First, we combine SQD with

the entanglement forging method (EF) [30], a scheme to represent a wavefunction of electrons in M spatial orbitals with M -qubit circuits, rather than the $2M$ -qubit circuits required by standard calculations. Second, we generalize the family of quantum circuits used in published literature about EF. Previous works focused on quantum circuits designed primarily for compatibility with noisy quantum devices, resulting in very limited accuracy. With improvements in error rates on quantum devices, and the introduction of QCSC algorithms like SQD, we reconsider the structure of the quantum circuits used in EF to achieve a more favorable compromise between hardware compatibility and accuracy.

II. METHODS

In this Section, we briefly review the SQD and EF methods. We then discuss their combination, and present a more general class of quantum circuits for electronic structure simulations using EF.

A. Sample-based quantum diagonalization (SQD)

SQD [25, 26] is a quantum subspace method [31] that uses a quantum circuit $|\Psi\rangle$ to sample a set of computational basis states $\chi = \{\mathbf{x}_1 \dots \mathbf{x}_d\}$ from the probability distribution $p(\mathbf{x}) = |\langle \mathbf{x} | \Psi \rangle|^2$ and a classical computer to solve the time-independent Schrödinger equation in the subspace spanned by the sampled computational basis states,

$$\sum_n H_{mn} c_n = E c_m, \quad H_{mn} = \langle \mathbf{x}_m | \hat{H} | \mathbf{x}_n \rangle. \quad (1)$$

In electronic structure applications, where a computational basis state parametrizes a Slater determinant, the matrix elements H_{mn} can be evaluated efficiently using a classical computer. Furthermore, because one needs to compute only a few eigenpairs and the matrix H is sparse and diagonally-dominated, Eq. (1) can be solved with Davidson's method.

We remark that (a) the spin-resolved particle number operators \hat{N}_σ (with $\sigma = \alpha, \beta$ for spin-up/down particles respectively) may not be conserved quantities, i.e. the sampled computational basis states may parametrize Slater determinants with incorrect number of spin-up/down electrons, and (b) the subspace spanned by the sampled computational basis states may not allow to produce eigenstates of the total spin operator \hat{S}^2 . Situation (a) may occur on noiseless quantum devices, if the quantum circuit $|\Psi\rangle$ breaks particle-number symmetries, and on noisy quantum devices, where computational basis states are sampled from a probability distribution $\tilde{p}(\mathbf{x})$ that differs from $p(\mathbf{x})$. Similarly, situation (b) may occur on noiseless and noisy quantum devices alike, because Slater determinants are generally not eigenstates of \hat{S}^2 .

To improve this scenario, SQD employs [26] an iterative self-consistent configuration recovery procedure. Each iteration has two inputs: a set of computational basis states χ sampled from a quantum device and an approximation to the unknown spin-resolved ground-state occupation number distribution $n_{p\sigma} = \langle \Psi_{\text{gs}} | \hat{a}_{p\sigma}^\dagger \hat{a}_{p\sigma} | \Psi_{\text{gs}} \rangle$. At each iteration,

1. for each sampled computational basis state with the wrong spin-resolved particle number, $\mathbf{x}_k \in \chi$, we compute the deviations $\Delta_{p\sigma}^k = |(x_k)_{p\sigma} - n_{p\sigma}|$ between the entries of \mathbf{x}_k and those of the occupation number distribution, and use them to define a probability distribution over the set of spin-orbitals $p\sigma$
2. we randomly flip a fixed number of 1s or 0s defined by the difference of the hamming weight of \mathbf{x}_k and desired number of electrons, according to the probability distribution in point 1, until the spin-resolved particle numbers assume target values, thereby producing a new set of recovered configurations χ_R
3. we sample K subsets (batches) from χ_R , that we call χ_b with $b = 1 \dots K$. Each batch yields a subspace \mathcal{S}_b of dimension d , in which we project the Hamiltonian as in Eq. (1), producing an approximation $E_b, |\psi_b\rangle$ to the ground eigenpair.
4. we use the lowest energy across batches, $\min_b E_b$, as the best approximation to the ground-state energy, and we use the states $|\psi_b\rangle$ to update the occupation number distribution,

$$n_{p\sigma} = \frac{1}{K} \sum_{b=1}^K \langle \psi_b | \hat{a}_{p\sigma}^\dagger \hat{a}_{p\sigma} | \psi_b \rangle. \quad (2)$$

5. we repeat points 1-4 until convergence of the energy $\min_b E_b$ and the occupation number distribution.

In the first iteration of configuration recovery, instead of points 1-2, we postselect [32] computational basis states in χ based on particle number. In the current formulation of SQD, total spin conservation can only be approximately enforced by adding a penalty term to the Schrödinger equation, that penalizes ground-state approximations with expectation value of \hat{S}^2 deviating from a target value.

B. Entanglement forging (EF)

EF [30, 33] is an algorithm to represent a $2M$ -qubit wavefunction as multiple M -qubit wavefunctions embedded in a classical computation. It is an example of a broader class of algorithms, including quantum embedding [34], that partition a system into a collection of weakly interacting clusters and correlate the results of each cluster to

reconstruct properties of the original system. EF considers wavefunctions of the form

$$|\Psi\rangle = \sum_{\mu} c_{\mu} |u_{\mu}\rangle \otimes |v_{\mu}\rangle. \quad (3)$$

In the original formulation, Eq. (3) is derived from a singular-value decomposition of a wavefunction, implying that the vectors u_{μ} and v_{μ} are orthonormal and the coefficients c_{μ} real and positive. For reasons of future convenience, we will consider non-orthogonal vectors and complex coefficients.

Eq. (3) allows to write expectation values of $2M$ -qubit operators starting from expectation values of M -qubit operators, e.g.

$$\langle \Psi | \hat{A} \otimes \hat{B} | \Psi \rangle = \sum_{\mu} |c_{\mu}|^2 a_{\mu} b_{\mu} + \sum_{\substack{pr=0 \\ \mu \neq \nu}} c_{\mu}^* c_{\nu} \gamma_{\mu\nu}^p \delta_{\mu\nu}^r a_{\mu\nu}^p b_{\mu\nu}^r \quad (4)$$

involving the following terms

$$\begin{aligned} a_{\mu} &= \langle u_{\mu} | \hat{A} | u_{\mu} \rangle, \quad a_{\mu\nu}^p = \langle u_{\mu\nu}^p | \hat{A} | u_{\mu\nu}^p \rangle, \\ b_{\mu} &= \langle v_{\mu} | \hat{B} | v_{\mu} \rangle, \quad b_{\mu\nu}^r = \langle v_{\mu\nu}^r | \hat{B} | v_{\mu\nu}^r \rangle, \end{aligned} \quad (5)$$

and the following normalized M -qubit states,

$$\begin{aligned} |u_{\mu\nu}^p\rangle &= \frac{|u_{\mu}\rangle + i^p |u_{\nu}\rangle}{U_{\mu\nu}^p}, \\ U_{\mu\nu}^p &= \sqrt{2 + 2 \text{Re}[i^p \langle u_{\mu} | u_{\nu} \rangle]}, \\ \gamma_{\mu\nu}^p &= \frac{(-i)^p (U_{\mu\nu}^p)^2}{4}, \end{aligned} \quad (6)$$

and

$$\begin{aligned} |v_{\mu\nu}^p\rangle &= \frac{|v_{\mu}\rangle + i^p |v_{\nu}\rangle}{V_{\mu\nu}^p}, \\ V_{\mu\nu}^p &= \sqrt{2 + 2 \text{Re}[i^p \langle v_{\mu} | v_{\nu} \rangle]}, \\ \delta_{\mu\nu}^p &= \frac{(-i)^p (V_{\mu\nu}^p)^2}{4}. \end{aligned} \quad (7)$$

Further simplifications, occurring e.g. if the coefficients c_{μ} are real and positive, are detailed in Ref. [30].

C. Combination between EF and SQD

In published literature, EF was used to compute expectation values while the central functionality of SQD is sampling from probability distributions. To combine SQD with EF, we introduce the projectors $|\mathbf{x}\rangle\langle\mathbf{x}|$ and $|\mathbf{y}\rangle\langle\mathbf{y}|$ acting on the two partitions in Eq. (4) to write the prob-

ability distribution $p(\mathbf{x}, \mathbf{y}) = |\langle \mathbf{x}, \mathbf{y} | \Psi \rangle|^2$ as

$$\begin{aligned} p(\mathbf{x}, \mathbf{y}) &= \sum_{\mu} |c_{\mu}|^2 p(\mathbf{x} | u_{\mu}) p(\mathbf{y} | v_{\mu}) \\ &+ \sum_{\substack{pr=0 \\ \mu \neq \nu}}^3 c_{\mu}^* c_{\nu} \gamma_{\mu\nu}^p \delta_{\mu\nu}^r p(\mathbf{x} | u_{\mu\nu}^p) p(\mathbf{y} | v_{\mu\nu}^r) \\ &= \sum_I r_I p_I(\mathbf{x}) q_I(\mathbf{y}) \end{aligned} \quad (8)$$

where $p(\mathbf{z} | \psi) = |\langle \mathbf{z} | \psi \rangle|^2$ is the probability to measure a length- M bitstring \mathbf{z} conditional to the preparation of an M -qubit register in the state $|\psi\rangle$. In the last line, we introduce the compact notation $\sum_I r_I p_I(\mathbf{x}) q_I(\mathbf{y})$ to avoid clutter. Eq. (8) is not a compound probability distribution, because the coefficients q_I are not, in general, a probability distribution. However, Eq. (8) may be approximated with a compound probability distribution of the form

$$\tilde{p}(\mathbf{x}, \mathbf{y}) = \sum_I P_I p_I(\mathbf{x}) q_I(\mathbf{y}) \quad (9)$$

where the coefficients $\{P_I\}_I$ are the entries of a probability distribution. Finding such probability distribution requires minimizing the log-likelihood function $\sum_{\mathbf{xy}} [p(\mathbf{x}, \mathbf{y}) - \tilde{p}(\mathbf{x}, \mathbf{y})]^2$ [35], which in turn requires knowledge of the inner products between the conditional probability distributions in Eq. (8). This information cannot be efficiently obtained by sampling, as it requires post-selection over measurement outcomes. Instead, in this study, we elected to use the approximation

$$P_I = \frac{\max [0, \text{Re}(r_I)]}{\sum_J \max [0, \text{Re}(r_J)]}. \quad (10)$$

This choice approximates the process of drawing samples from Eq. (8) through the process of drawing samples from Eq. (9). More specifically, fixing a total number N of shots, we can (i) sample the distribution P_I for N times and record the numbers N_I of times each of the I 's has been sampled, and (ii) sample each distribution $p_I(\mathbf{x}) q_I(\mathbf{y})$ for N_I times.

D. A more general family of EF wavefunctions

EF was used to simulate ground-state potential energy curves of H_2O [30], the activation energy of a Diels-Alder reaction [36], and the ground- and excited-state properties of H_3S^+ [37] and substituted aromatic heterocycles [38], in the framework of the variational quantum eigensolver (VQE) and quantum subspace expansion (QSE) based on single and double electronic excitation operators. In these studies, the states u_{μ} and v_{μ} in Eq. (3) were of the form

$$|u_{\mu}\rangle = |v_{\mu}\rangle = \prod_{(pr) \in S} v_{pr}(\theta_{pr}) |\mathbf{x}_{\mu}\rangle, \quad (11)$$

i.e. they resulted from the action, over a “bitstring state” $|\mathbf{x}_{\mu}\rangle$, of two-qubit gates called “hopgates” – here denoted $v(\theta)$ and acting on pairs (pr) of qubits in a set S . Such a choice, primarily dictated by compatibility with quantum device connectivity and coherence, resulted in low-accuracy simulations akin to multi-configurational self-consistent field (MCSCF) with 2-3 configurations, and prompted the use of expensive post-processing operations to increase accuracy. In this work, we consider a more general class of quantum circuits for EF calculations, beyond the combination of bitstring states and hopgates employed in published literature. Such circuits can be used in conventional EF calculations or in combination with SQD.

The starting point of this generalization is the observation that a suitable manipulation of a unitary coupled cluster doubles (uCCD) wavefunction yields a wavefunction that is very reminiscent of the EF state Eq. (3), albeit with clear differences in the structure of the wavefunctions $|u_{\mu}\rangle$ and $|v_{\mu}\rangle$, suggesting a natural and compelling generalization of Eq. (11). To this end, let us consider the uCCD wavefunction

$$|\Psi_{\text{uCCD}}\rangle = e^{\hat{T} - \hat{T}^{\dagger}} |\mathbf{x}_{\text{HF}}\rangle, \quad (12)$$

where $|\mathbf{x}_{\text{HF}}\rangle$ denotes the Hartree-Fock state (labeled by a bitstring in the basis of molecular orbitals), and

$$\begin{aligned} \hat{T} &= (t_{2\alpha\alpha})_{aibj} \hat{E}_{aibj}^{\alpha\alpha} + (t_{2\beta\beta})_{AIBJ} \hat{E}_{AIBJ}^{\beta\beta} \\ &+ (t_{2\alpha\beta})_{aiBJ} \hat{E}_{aiBJ}^{\alpha\beta} \\ &= \hat{T}_{\alpha\alpha} + \hat{T}_{\beta\beta} + \hat{T}_{\alpha\beta}. \end{aligned} \quad (13)$$

In the previous equation we used Einstein’s summation convention, labeled spin-up/down occupied orbitals with ij/IJ and spin-up/down virtual orbitals with ab/AB , and denoted excitation operators as

$$\hat{E}_{prqs}^{\sigma} = \hat{a}_{p\sigma}^{\dagger} \hat{a}_{q\sigma}^{\dagger} \hat{a}_{s\sigma} \hat{a}_{r\sigma}, \quad \hat{E}_{aiBJ}^{\alpha\beta} = \hat{a}_{a\alpha}^{\dagger} \hat{a}_{B\beta}^{\dagger} \hat{a}_{J\beta} \hat{a}_{i\alpha}. \quad (14)$$

With a simple manipulation (derived in Appendix A) one can write

$$\hat{T} - \hat{T}^{\dagger} = (\hat{T}_{\alpha\alpha} - \hat{T}_{\alpha\alpha}^{\dagger}) + (\hat{T}_{\beta\beta} - \hat{T}_{\beta\beta}^{\dagger}) + \sum_{\delta} \frac{\hat{X}_{\delta}^2}{2} \quad (15)$$

where \hat{X}_{δ} is a spin-unrestricted one-body operator. Employing a primitive Trotter approximation [39] and a Hubbard-Stratonovich transformation [40, 41],

$$e^{\frac{\hat{X}_{\delta}^2}{2}} = \int_{-\infty}^{\infty} dy_{\delta} \frac{e^{-\frac{y_{\delta}^2}{2}}}{\sqrt{2\pi}} e^{y_{\delta} \hat{X}_{\delta}}, \quad (16)$$

one can approximate the CCD wavefunction as

$$|\Psi_{\text{uCCD}}\rangle = \int d\mathbf{y} p(\mathbf{y}) \left(e^{\hat{T}_{\alpha\alpha} - \hat{T}_{\alpha\alpha}^{\dagger}} \otimes e^{\hat{T}_{\beta\beta} - \hat{T}_{\beta\beta}^{\dagger}} \right) |\Phi(\mathbf{y})\rangle \quad (17)$$

where $|\Phi(\mathbf{y})\rangle = e^{\sum_\delta y_\delta \hat{X}_\delta} |\mathbf{x}_{\text{HF}}\rangle$ is an unrestricted Slater determinant (see Appendix A for a derivation).

Eq. (17) is reminiscent of Eq. (3) and Eq. (11), with (a) an integral over continuous variables instead of a discrete summation, (b) a tensor product of unitary CCD operators instead of hopgates, and (c) non-orthogonal Slater determinants replacing “bitstring states”. It is also reminiscent of the representation of the imaginary-time evolution operator used in auxiliary-field quantum Monte Carlo [42, 43] calculations, although in that context the same-spin terms of the Hamiltonian are also subjected to a Hubbard-Stratonovich transformation.

Eq. (17) suggests a generalization of Eq. (11), where the states $|u_\mu\rangle$ and $|v_\mu\rangle$ have the form

$$\begin{aligned} |u_\mu\rangle &= e^{\hat{T}_{\alpha\alpha} - \hat{T}_{\alpha\alpha}^\dagger} e^{\hat{X}_\alpha^\mu} |\mathbf{x}_{\text{HF},\alpha}\rangle = e^{\hat{T}_{\alpha\alpha} - \hat{T}_{\alpha\alpha}^\dagger} |d_{\mu\alpha}\rangle, \\ |v_\mu\rangle &= e^{\hat{T}_{\beta\beta} - \hat{T}_{\beta\beta}^\dagger} e^{\hat{X}_\beta^\mu} |\mathbf{x}_{\text{HF},\beta}\rangle = e^{\hat{T}_{\beta\beta} - \hat{T}_{\beta\beta}^\dagger} |d_{\mu\beta}\rangle. \end{aligned} \quad (18)$$

In this equation, $\hat{X}_\sigma^\mu = \sum_{pr} X_{pr}^{\mu\sigma} \hat{a}_{ps}^\dagger \hat{a}_{r\sigma}$ is a one-body operator acting on spin- σ spin-orbitals, so the states $|d_{\mu\alpha}\rangle$ and $|d_{\mu\beta}\rangle$ are Slater determinants [44, 45].

When $\hat{T}_{\alpha\alpha} = \hat{T}_{\beta\beta} = 0$, the wavefunction Eq. (18) takes the form $\sum_\mu c_\mu |d_{\mu\alpha}\rangle \otimes |d_{\mu\beta}\rangle$ and reduces to resonating Hartree-Fock (ResHF) [46, 47] or the non-orthogonal configuration interaction (NOCI) [48–50] provided that the Slater determinants and coefficients are variationally optimized. Motivated by the relationship with ResHF and coupled-cluster theory, in this work we (i) define $|d_{\mu\alpha}\rangle \otimes |d_{\mu\beta}\rangle$ and c_μ using the output of a ResHF calculation, and (ii) define $\hat{T}_{\alpha\alpha}$ and $\hat{T}_{\beta\beta}$ using the output of a classical CCSD calculation (see Appendix A for additional details).

1. Quantum circuits

Implementing the EF wavefunction in Eq. (18) requires constructing quantum circuits to (i) prepare a Slater determinant, e.g. $|d_{\mu\alpha}\rangle$, or a superposition of Slater determinants, e.g.

$$|d_{\mu\nu\alpha}^p\rangle = \frac{|d_{\mu\alpha}\rangle + i^p |d_{\nu\alpha}\rangle}{U_{\mu\nu}^p}, \quad (19)$$

with $U_{\mu\nu}^p$ as in Eq. (6) and (ii) apply a uCCD operator. These circuits are shown in Fig. 2a, and described in detail in this Section.

a. *Slater determinants.* It is well known [51–54] that, in the standard Jordan-Wigner representation, the exponential of a one-body operator, e.g. \hat{X}_α^μ is implemented by a “Bogoliubov” quantum circuit. This circuit is exemplified in Fig. 2b and labeled $\text{Bog}(\hat{X}_\alpha^\mu)$. The Slater determinant $|d_{\mu\alpha}\rangle$ can be prepared by a more economical circuit [51–54] whose action on $|\mathbf{x}_{\text{HF},\alpha}\rangle$ coincides with that of $\text{Bog}(\hat{X}_\alpha^\mu)$, exemplified in Fig. 2b and labeled $\text{Slater}(\hat{X}_\alpha^\mu)$.

b. *Superpositions of Slater determinants.* Preparing a state of the form Eq. (19) is more subtle. First, let us write

$$|d_{\mu\nu\alpha}^p\rangle = \frac{I + i^p e^{\hat{X}_\alpha^{\mu\nu}}}{U_{\mu\nu}^p} |d_{\mu\alpha}\rangle, \quad (20)$$

where $e^{\hat{X}_\alpha^{\mu\nu}} = e^{\hat{X}_\alpha^\nu} e^{-\hat{X}_\alpha^\mu}$ is an orbital rotation. To apply the linear combination of unitaries $I + i^p e^{\hat{X}_\alpha^{\mu\nu}}$ to the state $|d_{\mu\alpha}\rangle$, one can use the quantum circuit in Fig. 2c (upper panel, see Appendix A for a proof). To implement the controlled orbital rotation, we recall that $\hat{X}_\alpha^{\mu\nu}$ is an anti-Hermitian operator and thus can be diagonalized by an orbital rotation \hat{W} , leading to

$$\mathbf{c} \left[e^{\hat{X}_\alpha^{\mu\nu}} \right] = \hat{W}^\dagger \mathbf{c} \left[e^{i \sum_q \xi_q \hat{a}_{q\alpha}^\dagger \hat{a}_{q\alpha}} \right] \hat{W}, \quad (21)$$

where ξ_q are the eigenvalues of $\hat{X}_\alpha^{\mu\nu}$ and $\mathbf{c}[\hat{U}] = |0\rangle\langle 0| \otimes I + |1\rangle\langle 1| \otimes \hat{U}$ denotes the controlled version of a quantum circuit. To implement the right-hand side of Eq. (21), we use the circuit shown in Fig. 2c (lower panel, see Appendix A for additional details).

c. *Unitary coupled-cluster.* Let us consider the same-spin CCD operators $\exp(\hat{T}_{\sigma\sigma} - \hat{T}_{\sigma\sigma}^\dagger)$. Through a low-rank decomposition of the t_2 amplitudes [55] and a Trotter approximation, these unitary operators can be written as

$$e^{\hat{T}_{\sigma\sigma} - \hat{T}_{\sigma\sigma}^\dagger} \simeq \prod_{\mu=1}^L e^{\hat{K}_\mu} e^{i \hat{J}_\mu} e^{-\hat{K}_\mu} \quad (22)$$

where the operators

$$\hat{K}_\mu = \sum_{pr} \kappa_{pr}^\mu(t_2) \hat{a}_{ps}^\dagger \hat{a}_{r\sigma}, \quad \hat{J}_\mu = \sum_{pr} J_{pr}^\mu(t_2) \hat{n}_{ps} \hat{n}_{r\sigma} \quad (23)$$

are determined by the t_2 amplitudes. The operators in Eq. (23) are, respectively, an orbital rotation and a “density-density interaction”. The latter can be implemented by a circuit of ZZ rotations with all-to-all connectivity. Eq. (22) motivated the unitary cluster Jastrow ansatz [56], in which the number of terms in the product can be chosen by the user rather than resulting from the t_2 amplitudes and the number of steps in the Trotter approximation, and the local unitary cluster Jastrow (LUCJ) ansatz [57], in which the density-density operators \hat{J}_μ requiring all-to-all qubit connectivity or costly SWAP networks [58] are truncated by replacing the dense matrix J_{pr}^μ with a sparse matrix. While, in near-term implementation, the only elements of J_{pr}^μ are those that may be implemented without any SWAP networks (see Fig. 2b for an example), as error rates on quantum devices decrease, one may consider a hierarchy of increasingly dense matrices converging towards the UCJ limit (e.g. banded matrices). The quantum circuits that implement the LUCJ ansatz with $L = 1$ are shown in Fig. 2a.

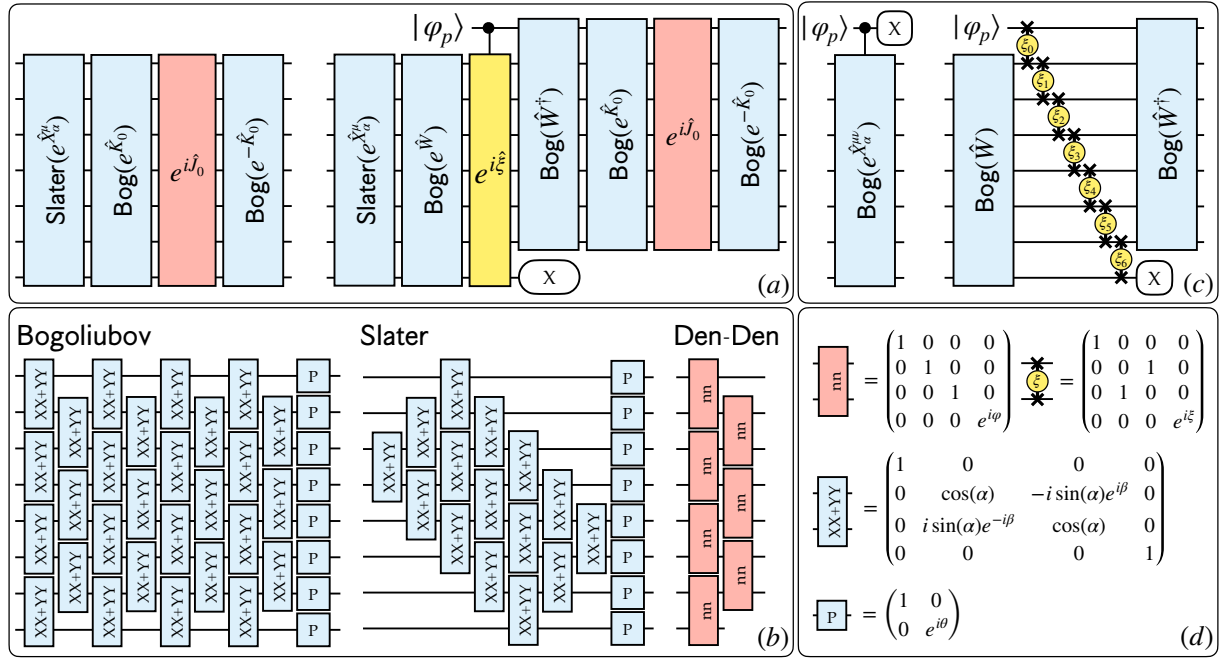


FIG. 2: (a) Quantum circuits to prepare the states u_μ (left) and $u_{\mu\nu}^p$ (right), with $|\varphi_p\rangle = \frac{|0\rangle + i^p|1\rangle}{\sqrt{2}}$. (b) Compilation of an orbital rotation (left) and a quantum circuit to prepare a Slater determinant (middle) into XX+YY and phase gates (blue symbols) and of a density-density interaction (abbreviated “Den-Den”) into number-number gates with linear qubit connectivity (right, red symbols). (c) quantum circuit to apply a controlled orbital rotation (left) and its compilation into orbital rotations and the controlled exponential of a diagonal one-body operator (right). (d) Definition of one- and two-qubit gates in panels (a)-(c).

	qubits	XX+YY	nn	depth
LUCJ	$2M$	$\sum_\sigma N_\sigma(M - N_\sigma) + L\{2M(M - 1)\}$	$L\{2(M - 1) + \frac{M}{4}\}$	$(M - 1) + L\{M + 3\}$
EF (ind)	M	$N_\sigma(M - N_\sigma) + L\{M(M - 1)\}$	$L\{2(M - 1) + \frac{M}{4}\}$	$(M - 1) + L\{M + 2\}$
EF (super)	M	$N_\sigma(M - N_\sigma) + (M + 1)(M - 1) + L\{M(M - 1)\}$	$L\{(M - 1)\}$	$3(M - 1) + L\{M + 2\}$

TABLE I: Quantum resources to execute a standard LUCJ circuit on a lattice with heavy-hex qubit connectivity (first row) and to prepare the individual states u_μ , v_μ and the superposition states $u_{\mu\nu}^p$, $v_{\mu\nu}^r$ in EF (second and third row, labeled “ind” and “super” respectively). M , N_σ , and L denote the number of spin- σ electrons, spatial orbitals, and layers of the LUCJ circuit, respectively.

d. Quantum resource estimate Quantum resources (number of qubits, number of 2-qubit XX+YY and nn gates, and depth of the 2-qubit gate) to execute standard LUCJ and EF circuits are listed in Table I. Circuits for preparing individual states u_μ , v_μ have roughly half the gates of standard LUCJ circuits and a marginally lower depth. Circuits for preparing superposition states $u_{\mu\nu}^p$, $v_{\mu\nu}^r$ have roughly half the gates of standard LUCJ circuits plus $(M + 1)(M - 1)$ additional gates and higher depth, specifically $2(M - 1)$ more layers of two-qubit gates. Since the $(M + 1)(M - 1)$ additional gates roughly correspond to the cost of a Bogoliubov circuit, the standard LUCJ circuit has more gates for $L \geq 2$. The decreased qubit count, compared to standard LUCJ, gives more freedom in the choice of the qubit layout and protection against cross-talk errors.

E. Target reaction

This study is motivated by the photo-oxidation of the epoxy resin DGEBA [59]. This process is a multi-step chain reaction [60], described in detail in Appendix C, comprising a propagation phase in which a radical from the environment abstracts a hydrogen from a primary methyl group on the DGEBA subunit. Rivaton et al [59] conjectured that the radical driving this hydrogen abstraction chain is a CH_3^\bullet generated by an earlier photolytic dissociation process. This observation pinpoints the importance of accurately computing the activation energy for a reaction of the form $\text{XCH}_3 + \text{CH}_3^\bullet = \text{XCH}_2^\bullet + \text{CH}_4$, where XCH_3 denotes the DGEBA molecule, in order to understand the photodissociation process as a whole [61].

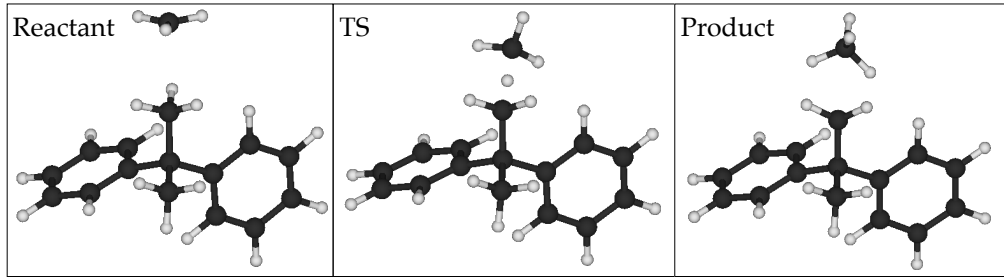


FIG. 3: Left to right: reactant, transition state, and product geometries for the hydrogen abstraction reaction considered in this study.

In this study, we consider a simplified structure possessing similar physical and chemical properties to DGEBA, specifically 2,2-Diphenylpropane [62]. While this simplified structure lacks the epoxide group present in DGEBA, we assume hydrogen abstraction from a central methyl group, the reaction of interest, is not significantly influenced by the presence or absence of the epoxide on the ends of the molecule. To determine the reaction path of our radical model, we used density functional theory (DFT) with the B3LYP functional [63] and D3 dispersion corrections [64] at the cc-PVDZ [65] level of theory as implemented in the Schrödinger software [66]. We evaluated and optimized the energies of candidate reactant, transition state, and product geometries, obtaining the results in Fig. 3. We located the saddle point indicating the transition state using the Quadratic Synchronous Transit (QST) method as implemented in Schrödinger. For the minima and transition-state searches, we fixed the distance between the carbon atoms of the CH_3 radical and the methyl group involved in hydrogen abstraction to $R_{\text{C}-\text{C}} = 2.69 \text{ \AA}$.

1. Classical pre-processing

We compute the activation energy $\Delta E^\ddagger = E_{\text{TS}} - E_{\text{R}}$ and the reaction energy $\Delta E = E_{\text{P}} - E_{\text{R}}$ in two different active spaces of sizes (13e,13o) and (23e,23o). These active spaces are spanned by intrinsic bond orbitals [67] located around CH_3^\bullet and CH_4 where hydrogen abstraction occurs for the active space (13e,13o) and around additional neighboring atoms, as shown in Fig. 4 for the active spaces (23e,23o). Both active spaces have one additional alpha electron compared to the beta electrons. The reason for considering two different active spaces is to assess the performance of the combination between SQD and EF across multiple system sizes. In each active space, we used the classical methods restricted open-shell Hartree-Fock (ROHF), coupled-cluster singles and doubles (CCSD), and CCSD with perturbative triples (CCSD(T)), as implemented in the PySCF software package [68, 69]. We also used the heat-bath configuration interaction (HCI) as implemented in the DICE package [70] – working in the basis of CCSD natural or-

bitals and using truncation thresholds of 10^{-7} , $5 \cdot 10^{-6}$, and $5 \cdot 10^{-5}$ a.u. for the active spaces – and the density matrix renormalization group (DMRG) as implemented in the Block2 package [71] – using a bond dimension of 4000, SU(2) symmetry, and working in the basis of CCSD natural orbitals ordered by a genetic algorithm.

2. Details of quantum simulations

We constructed the EF quantum circuits using the open-source ffsim library [54] and an in-house code to supply the circuit parameters based on classical CCSD and ResHF calculations. We executed these quantum circuits on IBM’s 133-qubit Heron superconducting quantum processor `ibm_torino`, gathering 500000 measurement outcomes for each circuit.

After executing the EF quantum circuits, we collated the measurement outcomes from the individual circuits as discussed in Section II C. We then used SQD to approximate molecular eigenstates, as implemented in IBM’s SQD addon package [72].

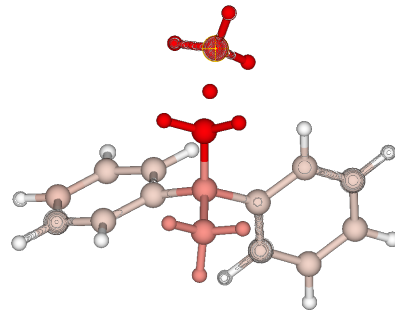


FIG. 4: Active-space selection, exemplified for the transition-state geometry. Intrinsic bond orbitals (IBOs) are constructed, and those localized around the atoms in red (the CH_3^\bullet and CH_4 where the hydrogen abstraction occurs) define the (13e,13o) active space. Similarly, IBOs localized around the atoms in red and dark pink define the (23e,23o) active space.

III. RESULTS

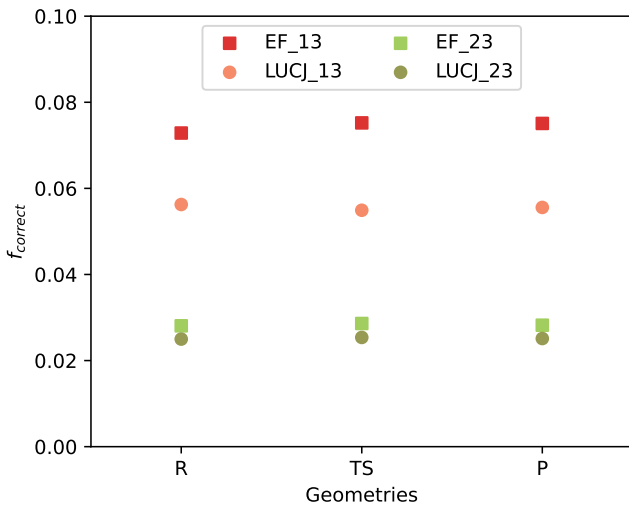


FIG. 5: Fraction of measured binary strings with correct number of spin-up/down electrons, from EF and LUCJ quantum circuits (squares and circles, respectively) prepared on quantum hardware, for different active spaces (red, green, blue for (13e,13o) and (23e,23o) active spaces, respectively) and geometries (left to right: reactant, transition states, marked R, TS, and P respectively).

In Fig. 5, we report the fraction, f_{correct} , of obtaining counts with the right number of alpha and beta electrons for the different active space sizes. To calculate f_{correct} for the EF circuits, we averaged the fraction of getting the right number of alpha(beta) electrons from the EF (ind) and EF (super) circuits and reported the product of the averages. We compare this fraction with the counts obtained from the EF circuits and the LUCJ circuits. Across all the active space sizes and geometries (reactant, transition state, and product), we observe that f_{correct} for EF circuits is larger than the corresponding value for LUCJ circuits. The difference is more pronounced for smaller active space of (13e,13o). In Table II, we provide information about the total number of qubits including ancilla qubits, two-qubit gates, and circuit depths for the EF and LUCJ circuits after transpilation to the HW. We see that the required 2 qubit gates and circuit depths are significantly smaller for the EF circuits when compared to the LUCJ circuits.

For each geometry we run $K = 5$ independent SQD calculations also called batches with N_{spb} samples per batch and 5 self-consistent configuration recovery iterations. Minimum energy across iterations and batches are reported. In Fig. 6, we show the ground-state energy of reactant, transition state, and product in a (13e,13o) active space. The SQD energy is computed by diagonalizing the Hamiltonian in subspaces spanned by D configurations which is controlled by N_{spb} . As expected, the SQD

circuit	qubits (system + ancilla)	2-qubit gates (cz)	depth
(13e,13o) EF (ind)	13	248	257
(13e,13o) EF (super)	13+1	450	474
(13e,13o) LUCJ	26+4	1606	631
(23e,23o) EF (ind)	23	800	434
(23e,23o) EF (super)	23+1	1375	834
(23e,23o) LUCJ	46+6	5167	1222

TABLE II: Quantum resources to execute individual (ind) and superposition (super) EF circuits and standard LUCJ circuits after transpilation on devices with heavy-hex topology. Numbers reported for the two-qubit gates and depth are averaged over the spin-up and spin-down circuits (for EF) as well as geometries (for EF and LUCJ).

energy decreases as N_{spb} increases, since increasing N_{spb} leads to higher D . For all values of N_{spb} we studied, the SQD energy is below CISD and, for $N_{\text{spb}} \simeq 5000$ which gives a subspace dimension of $D \simeq 1.3 * 10^6$, it agrees well with CCSD, CCSD (T), HCl and DMRG within 1 kcal/mol.

In Fig. 7, we instead consider a (23e,23o) active space. As seen, in this larger active space, the SQD energy is comparable or lower than CISD with $N_{\text{spb}} = 35000$ which gives $D \simeq 3.9 * 10^8$ dimensional subspace. This is roughly 20 kcal/mol above CCSD, CCSD (T), HCl and DMRG for all three geometries.

In Fig. 8 we consider the activation energy $E_{\text{TS}} - E_{\text{R}}$ and the reaction energy $E_{\text{P}} - E_{\text{R}}$. As seen, CCSD, CCSD(T), HCl, and DMRG agree well within 1 kcal/mol for these energy differences in all the active spaces considered (with the exception of HCl in the largest active space). On the other hand, RHF, MP2, and CISD overestimate the activation energy for all active spaces. The performance of SQD is visibly dependent on the active-space size: for (13e,13o), where SQD delivers near-exact results, energy differences are naturally in excellent agreement with CCSD, CCSD(T), HCl, and DMRG. For (23e,23o), where SQD energies are of accuracy comparable with CISD, the activation energy is slightly overestimated but still in closer agreement with CCSD, CCSD(T), HCl, and DMRG than RHF, MP2, and CISD due to a cancellation of errors.

IV. CONCLUSION AND OUTLOOK

In this work, we combined the entanglement forging (EF) and sample-based quantum diagonalization (SQD) methods. The main difficulty posed by this integration is that the probability distribution of the electronic configuration over an EF wavefunction, Eq. (8), is not a compound probability distribution. To overcome this difficulty, we proposed to sample configurations from an approximate compound probability distribution, Eq. (9). To increase

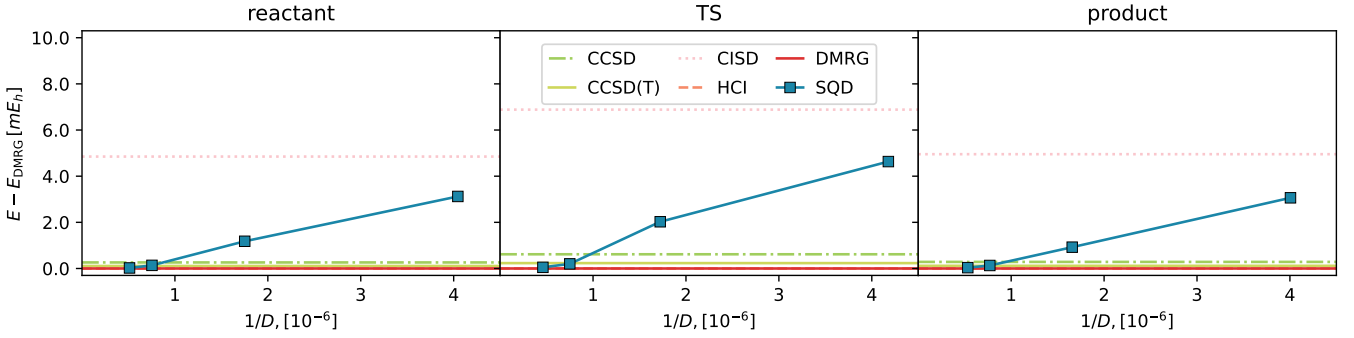


FIG. 6: Deviation between SQD and DMRG energy (blue squares) as a function of the subspace dimension for reactant, transition state, and product (left to right) in a (13e,13o) active space, and classical methods (horizontal lines).

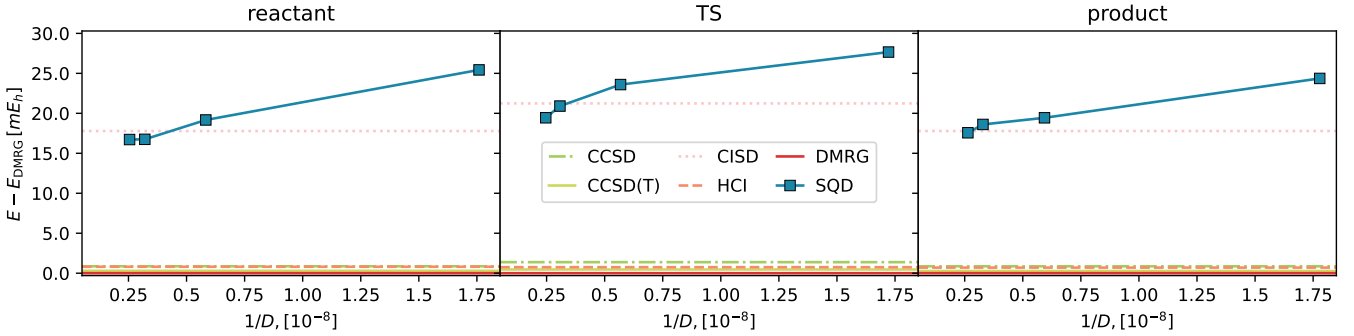


FIG. 7: Deviation between SQD and DMRG energy (blue squares) as a function of the subspace dimension for reactant, transition state, and product (left to right) in a (23e,23o) active space, and classical methods (horizontal lines).

the flexibility of EF, both in variational and SQD simulations, we proposed a more general family of EF wavefunction, wherein linear combinations of nonorthogonal Slater determinants and an approximate unitary coupled-cluster wavefunction (called local unitary cluster Jastrow or LUCJ) replace the “bistrings” (i.e., individual electronic configurations) and hopgates (i.e., two-qubit gates) used in previous studies. The choice of non-orthogonal Slater determinants and an approximate unitary coupled-cluster wavefunction is motivated by a connection between EF and coupled-cluster theory, revealed by a Hubbard-Stratonovich transformation.

The quantum circuits required by the combination of SQD and EF are divided into: diagonal (for the preparation of a Slater determinant and the application of an LUCJ circuit) and superposition (for the preparation of a linear combination of two Slater determinants and the application of an LUCJ circuit). The former have $\sim 50\%$ the qubits and quantum gates of an equivalent LUCJ circuit and slightly lower depth. The latter, due to an economization of the “Hadamard test” circuit for the preparation of superpositions of Slater determinants, have $(M+1)(M-1)$ additional gates and $2(M-1)$ more layers of two-qubit gates. As such, they are always deeper

than a conventional LUCJ circuit and have fewer gates for $L \geq 2$ repetitions. We note that EF circuits – having half the qubits than conventional circuits and requiring linear connectivity in this case – may be executed in parallel and benefit from more freedom in the choice of qubit layout.

We used the combination of EF and SQD to simulate the activation energy and reaction energy of a hydrogen abstraction reaction motivated by photodegradation of composite polymers, in active spaces of (13e, 13o) and (23e, 23o), to assess the performance of the method with increasing numbers of active electrons and orbitals. As the electronic wavefunctions along the steps of the reaction are dominated by the mean-field configuration (i.e. electron correlation is purely dynamical), we used different classical methods – CCSD(T), HCl, and DMRG – to provide reference results against which to compare EF. For the (13e,13o) active space, SQD + EF provided results of accuracy comparable to reference classical methods, see Fig. 6. For the (23e,23o) active space, on the other hand, it produced total energies of CISD-like quality (some ~ 20 kcal/mol above reference classical results, see Fig. 7). However, due to a cancellation of errors, they produced an activation energy and a reaction energy ~ 2

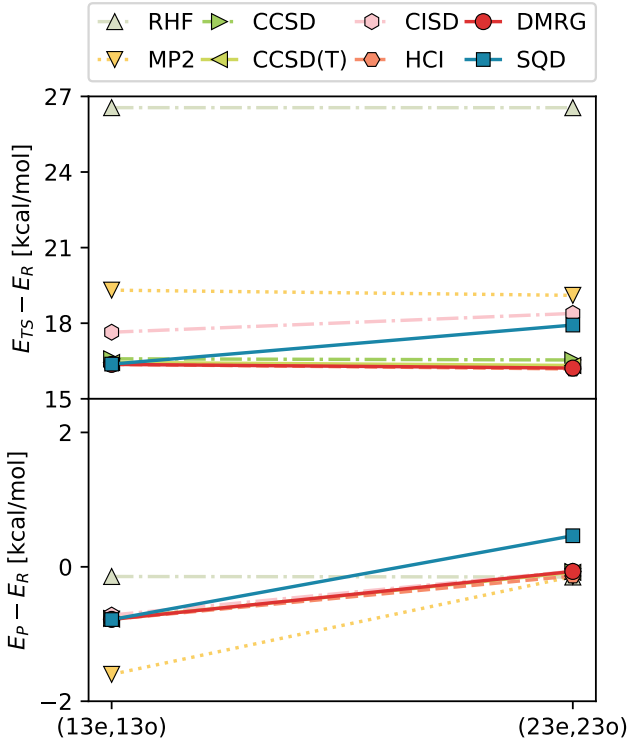


FIG. 8: Activation energy $E_{TS} - E_R$ and reaction energy $E_P - E_R$ from classical methods and SQD, using active spaces of (13e,13o) and (23e,23o).

kcal / mol away from the classical reference results.

This work may be continued and refined in different ways. First, by optimizing free parameters in the EF wavefunction – both in quantum circuits and in the probabilities P_I in Eq. (9) – to minimize the SQD energy [25]. Second, by moving beyond hydrogen abstraction towards other molecular species, including with multireference electronic character, e.g., to perform a systematic assessment of accuracy. Finally, the techniques presented here may be a starting point to combine SQD with circuit knitting techniques [73].

Appendix A: Additional details about EF

In this Section, we derive Eq. (15) and Eq. (17) of the main text, and provide more information about the parameterization of Eq. (18).

Let us start by performing a singular-value decomposi-

tion (SVD) of the opposite-spin t_2 amplitudes in Eq. (13),

$$\begin{aligned}
 \hat{T}_{\alpha\beta} &= \sum_{aiBJ} (t_{2\alpha\beta})_{aiBJ} \hat{E}_{ai}^\alpha \hat{E}_{BJ}^\beta \\
 &= \sum_s \tau_s \sum_{aiBJ} U_{ai}^s V_{BJ}^s \hat{E}_{ai}^\alpha \hat{E}_{BJ}^\beta \\
 &= \sum_s \left[\sum_{ai} \sqrt{\tau_s} U_{ai}^s \hat{E}_{ai}^\alpha \right] \left[\sqrt{\tau_s} \sum_{BJ} V_{BJ}^s \hat{E}_{BJ}^\beta \right] \\
 &= \sum_s \hat{u}_s \hat{V}_s = \sum_s \frac{(\hat{u}_s + \hat{V}_s)^2 + (i\hat{u}_s - i\hat{V}_s)^2}{4}.
 \end{aligned} \tag{A1}$$

Since the \hat{u}_s and \hat{V}_s commute, we can write

$$\begin{aligned}
 \hat{T}_{\alpha\beta} - \hat{T}_{\alpha\beta}^\dagger &= \frac{1}{4} \sum_s (\hat{u}_s + \hat{V}_s)^2 + (i\hat{u}_s - i\hat{V}_s)^2 \\
 &\quad + \frac{1}{4} \sum_s (i\hat{u}_s^\dagger + i\hat{V}_s^\dagger)^2 + (\hat{u}_s^\dagger - \hat{V}_s^\dagger)^2
 \end{aligned} \tag{A2}$$

and this equation defines the squares of one-body operators in Eq. (15). To prove Eq. (17), we consider the following Trotter approximation

$$e^{\hat{T} - \hat{T}^\dagger} \simeq e^{\hat{T}_{\alpha\alpha} - \hat{T}_{\alpha\alpha}^\dagger} e^{\hat{T}_{\beta\beta} - \hat{T}_{\beta\beta}^\dagger} \prod_\delta e^{\frac{\hat{X}_\delta^2}{2}}. \tag{A3}$$

We then use the Hubbard-Stratonovich representation to obtain

$$e^{\hat{T} - \hat{T}^\dagger} \simeq e^{\hat{T}_{\alpha\alpha} - \hat{T}_{\alpha\alpha}^\dagger} e^{\hat{T}_{\beta\beta} - \hat{T}_{\beta\beta}^\dagger} \prod_\delta \int_{-\infty}^{\infty} dy_\delta \frac{e^{-\frac{y_\delta^2}{2}}}{\sqrt{2\pi}} e^{y_\delta \hat{X}_\delta}. \tag{A4}$$

Let us now introduce the approximation

$$\prod_\delta e^{y_\delta \hat{X}_\delta} \simeq e^{\sum_\delta y_\delta \hat{X}_\delta} \tag{A5}$$

and the definitions $\mathbf{y} = \{y_\delta\}_\delta$ and $p(\mathbf{y}) = \prod_\delta \frac{e^{-\frac{y_\delta^2}{2}}}{\sqrt{2\pi}}$, obtaining

$$e^{\hat{T} - \hat{T}^\dagger} \simeq e^{\hat{T}_{\alpha\alpha} - \hat{T}_{\alpha\alpha}^\dagger} e^{\hat{T}_{\beta\beta} - \hat{T}_{\beta\beta}^\dagger} \prod_\delta \int d\mathbf{y} p(\mathbf{y}) e^{\sum_\delta y_\delta \hat{X}_\delta}, \tag{A6}$$

from which Eq. (17) immediately follows.

To define the wavefunctions in Eq. (18), we use a two-step procedure.

- First, we perform a CCSD calculation yielding amplitudes $t_{2\alpha\alpha}$, $t_{2\beta\beta}$, and $t_{2\alpha\beta}$, and we use the same-spin amplitudes to parametrize the LUCJ circuit as detailed in the supplementary information of Ref. [26].
- Second, we perform a ResHF calculation to define the determinants $d_{\mu\sigma}$ and coefficients c_μ . We solve the ResHF equations as defined in Ref. [47], using the following “warm-starting” procedure to provide initial orbitals and coefficients:

1. we choose a number of determinants N_{det} ,
2. we sample N_{det} auxiliary fields $\{\mathbf{y}_\mu\}_{\mu=1}^{N_{\text{det}}}$ from the normal distribution in Eq. (17) defining Slater determinants $|\Phi(\mathbf{y}_\mu)\rangle$,
3. we variationally optimize $\sum_\mu c_\mu |\Phi(\mathbf{y}_\mu)\rangle$ with respect to c_μ and \mathbf{y}_μ . More specifically, we define $\tilde{c}_\mu(\mathbf{y})$ as the lowest-energy solution of $\sum_\mu \langle \Phi(\mathbf{y}_\nu) | \hat{H} | \Phi(\mathbf{y}_\mu) \rangle \tilde{c}_\mu(\mathbf{y}) = E_0(\mathbf{y})$ $\sum_\mu \langle \Phi(\mathbf{y}_\nu) | \Phi(\mathbf{y}_\mu) \rangle \tilde{c}_\mu(\mathbf{y})$ and minimize $E_0(\mathbf{y})$ as a function of \mathbf{y} . We use the resulting linear combination of non-orthogonal determinants as the initial point of the variational optimization in Ref. [47].

Appendix B: Additional details about quantum circuits

In this Section, we show that the circuits in Fig. 2c prepare the superposition state in Eq. (20). First, a register of qubits prepared in $|d_{\mu\alpha}\rangle$ is coupled to an ancilla prepared in the state $|\varphi_p\rangle = \frac{|0\rangle + i^p|1\rangle}{\sqrt{2}}$. Then, the controlled operation

$$\mathbf{c}[e^{\hat{X}_\alpha^{\mu\nu}}] = |0\rangle\langle 0| \otimes I + |1\rangle\langle 1| \otimes e^{\hat{X}_\alpha^{\mu\nu}} \quad (\text{B1})$$

is applied, producing the output state

$$\begin{aligned} |0\rangle|d_{\mu\alpha}\rangle + i^p|1\rangle|d_{\nu\alpha}\rangle &= |+\rangle \left[\frac{|d_{\mu\alpha}\rangle + i^p|d_{\nu\alpha}\rangle}{\sqrt{2}} \right] \\ &+ |-\rangle \left[\frac{|d_{\mu\alpha}\rangle + i^p|d_{\nu\alpha}\rangle}{\sqrt{2}} \right]. \end{aligned} \quad (\text{B2})$$

Recalling Eq. (6), we can write this equation as

$$|0\rangle|d_{\mu\alpha}\rangle + i^p|1\rangle|d_{\nu\alpha}\rangle = \frac{U_{\mu\nu}^p}{\sqrt{2}}|+\rangle|d_{\mu\nu\alpha}^p\rangle + \frac{U_{\mu\nu}^{p+2}}{\sqrt{2}}|-\rangle|d_{\mu\nu\alpha}^{p+2}\rangle \quad (\text{B3})$$

The ancilla is then measured in the Pauli X basis, yielding results ± 1 with probabilities

$$p(1) = \frac{1}{2} [U_{\mu\nu}^p]^2, \quad p(-1) = \frac{1}{2} [U_{\mu\nu}^{p+2}]^2 \quad (\text{B4})$$

and collapsing the main register in the states $|d_{\mu\nu\alpha}^p\rangle$ and $|d_{\mu\nu\alpha}^{p+2}\rangle$ respectively. Note that, while the preparation of $|d_{\mu\nu\alpha}^p\rangle$ is probabilistic, measurement outcomes need not be discarded, because the EF method also requires the preparation of $|d_{\mu\nu\alpha}^{p+2}\rangle$.

So far, we verified that the circuit in the top portion of Fig. 2c prepares the state $|d_{\mu\nu\alpha}^p\rangle$. The controlled operation $\mathbf{c}[e^{\hat{X}_\alpha^{\mu\nu}}]$, if implemented naively, can be considerably expensive, leading to a circuit of $O(M^2)$ controlled two-qubit gates requiring all-to-all qubit connectivity. To

achieve a more economic implementation, we recall that $\hat{X}_\alpha^{\mu\nu} = \sum_{pr} X_{pr}^{\mu\nu} \hat{a}_{p\alpha}^\dagger \hat{a}_{r\alpha}$ is an anti-Hermitian one-body operator, and thus can be diagonalized by an orbital rotation $\hat{W} = \sum_{pr} W_{pr} \hat{a}_{p\alpha}^\dagger \hat{a}_{r\alpha}$ with $\sum_r X_{pr}^{\mu\nu} W_{rq} = i\xi_q W_{pq}$. We can then write

$$\mathbf{c}[e^{\hat{X}_\alpha^{\mu\nu}}] = \hat{W}^\dagger \mathbf{c}[e^{\sum_q i\xi_q \hat{a}_{q\alpha}^\dagger \hat{a}_{q\alpha}}] \hat{W}. \quad (\text{B5})$$

Since, in the Jordan-Wigner representation, $\hat{a}_{q\alpha}^\dagger \hat{a}_{q\alpha} = |1\rangle\langle 1|_q$, the controlled operation $\mathbf{c}[e^{\sum_q i\xi_q \hat{a}_{q\alpha}^\dagger \hat{a}_{q\alpha}}]$ is a product of M controlled single-qubit Z rotations. While these controlled operations require all-to-all connectivity, we can easily implement them on a device with linear qubit connectivity by swapping the ancilla from the first to the last position of the register, i.e.

$$\mathbf{c}[e^{\hat{X}_\alpha^{\mu\nu}}] = \hat{W}^\dagger \prod_{q=1}^M \mathbf{c}_{q-1} \text{SWAP}_{q-1,q} \mathbf{c}_{q-1} [e^{i\xi_q |1\rangle\langle 1|}] \hat{W}. \quad (\text{B6})$$

as shown in Fig. 2c – d, where a circle traversed by a vertical line delimited by two crosses denotes a gate $\text{SWAP}_{q-1,q} \mathbf{c}_{q-1} [e^{i\xi_q |1\rangle\langle 1|}]$.

Appendix C: Additional details about the target reaction

This study is motivated by the photo-oxidation of the epoxy resin DGEBA [74]. The free-radical mechanism of photo-oxidative degradation is a multistep chain reaction [60]. First, incident UV and visible-light radiation excites chromophoric groups within the epoxy resin (e.g. aromatic rings). This excitation causes a homolytic dissociation and the formation of radicals, which subsequently abstract hydrogens from other epoxy polymers, leading to further scission and propagation steps [75]. The precise mechanisms after radical formation proposed by Rivaton *et al.* [59] proceed in three steps [59, 76], illustrated in Fig. 9. First, hydrogen abstraction occurs, in which a carbon-hydrogen bond within one of the CH_3 groups undergoes homolytic dissociation, leaving the DGEBA molecule with one less hydrogen atom (through the modification of the methyl groups CH_3 to CH_2^\bullet). Then an isomerization reaction occurs in which the constituents of the molecule are rearranged. Finally, interactions with UV and visible light cause a scission reaction that breaks DGEBA into an alcohol molecule and quinone methide, producing a strong absorption peak at 340 nm and a second peak in the IR spectrum at 6035 nm (1657 cm^{-1}). As the first step after radical formation in the proposed mechanism of photodegradation of the DGEBA epoxy resin is hydrogen abstraction, computing the activation energy for this process is crucial to understanding the reaction as a whole [61].

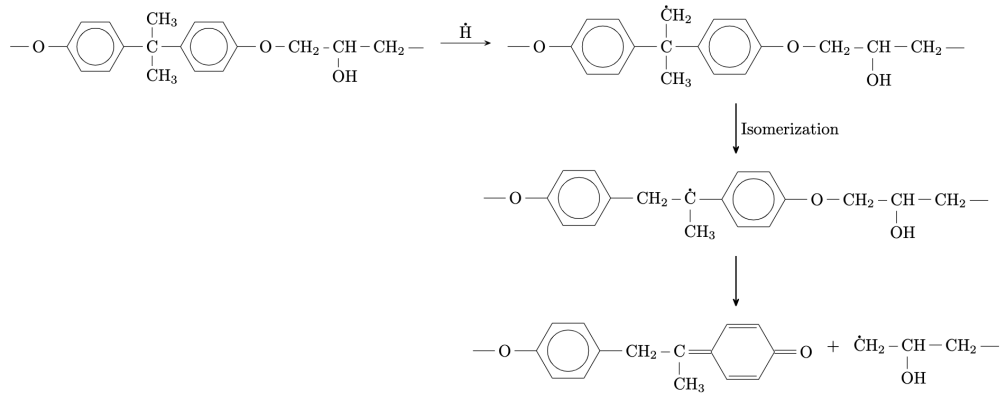


FIG. 9: Key photodegradation reactions for DGEBA epoxy resin.

[1] P. Mangalgiri, Composite materials for aerospace applications, *Bull. Mater. Sci.* **22**, 657 (1999).

[2] K. B. Mahat, I. Alarifi, A. Alharbi, and R. Asmatulu, Effects of UV light on mechanical properties of carbon fiber reinforced pps thermoplastic composites, in *Macromolecular Symposia*, Vol. 365 (Wiley Online Library, 2016) pp. 157–168.

[3] D. Jung, Y. Mizutani, A. Todoroki, and W. Na, Effect of ultraviolet irradiation on the material properties and acoustic emission of a fiber-reinforced composite, *Fibers and Polymers* **22**, 1940 (2021).

[4] T. S. Gates, *On the use of accelerated test methods for characterization of advanced composite materials* (National Aeronautics and Space Administration, Langley Research Center, 2003).

[5] A. Rezig, T. Nguyen, D. Martin, L. Sung, X. Gu, J. Jasmim, and J. W. Martin, Relationship between chemical degradation and thickness loss of an amine-cured epoxy coating exposed to different UV environments, *J. Coat. Technol. Res* **3**, 173 (2006).

[6] U. Schulz, Accelerated testing: Nature and artificial weathering in the coatings industry, vinzentz network gmbh & co, **KG, Hannover, Germany** (2009).

[7] U.s. dot/faa - decision faa-2022-1397-0006.

[8] B. Parveez, M. Kittur, I. A. Badruddin, S. Kamangar, M. Hussien, and M. Umarfarooq, Scientific advancements in composite materials for aircraft applications: a review, *Polymers* **14**, 5007 (2022).

[9] Y. Zhu, K. Cao, M. Chen, and L. Wu, Synthesis of uv-responsive self-healing microcapsules and their potential application in aerospace coatings, *ACS applied materials & interfaces* **11**, 33314 (2019).

[10] S. M. Arnold, D. Cebon, and M. Ashby, *Materials selection for aerospace systems*, Tech. Rep. (2012).

[11] K. Jayakrishna, V. R. Kar, M. T. Sultan, and M. Rakesh, Materials selection for aerospace components, in *Sustainable composites for aerospace applications* (Elsevier, 2018) pp. 1–18.

[12] D. B. Miracle, S. L. Donaldson, S. D. Henry, C. Moosbrugger, G. J. Anton, B. R. Sanders, N. Hrivnak, C. Terrian, J. Kinson, K. Muldoon, *et al.*, *ASM handbook*, Vol. 21 (ASM international Materials Park, OH, 2001).

[13] A. Quilter, Composites in aerospace applications, *IHS White Paper* **444**, 264 (2001).

[14] T. Lu, E. Solis-Ramos, Y. Yi, and M. Kumosa, Uv degradation model for polymers and polymer matrix composites, *Polym. Degrad. Stab* **154**, 203 (2018).

[15] S. Kiil, Model-based analysis of photoinitiated coating degradation under artificial exposure conditions, *J. Coat. Technol. Res* **9**, 375 (2012).

[16] M. Evans, A statistical degradation model for the service life prediction of aircraft coatings: With a comparison to an existing methodology, *Polymer Testing* **31**, 46 (2012).

[17] X. Meng, G. Jin, and R. Yang, A quantum chemical and molecular dynamics simulation study on photo-oxidative aging of polyethylene: Mechanism and differences between crystalline and amorphous phases, *Polym. Degrad. Stab* **217**, 110536 (2023).

[18] T. P. Gujarati, M. Motta, T. N. Friedhoff, J. E. Rice, N. Nguyen, P. K. Barkoutsos, R. J. Thompson, T. Smith, M. Kagele, M. Brei, *et al.*, Quantum computation of reactions on surfaces using local embedding, *npj Quantum Inf* **9**, 88 (2023).

[19] J. L. Smialek, N. S. Jacobson, *et al.*, Oxidation of high-temperature aerospace materials, *High temperature materials and mechanisms* , 95 (2014).

[20] Z. Shi, C. Zou, F. Zhou, and J. Zhao, Analysis of the mechanical properties and damage mechanism of carbon fiber/epoxy composites under uv aging, *Materials* **15**, 2919 (2022).

[21] R. de Borst, Challenges in computational materials science: Multiple scales, multi-physics and evolving discontinuities, *Computational Materials Science* **43**, 1 (2008), proceedings of the 16th International Workshop on Computational Mechanics of Materials.

[22] N. Sai, K. Leung, J. Zádor, and G. Henkelman, First principles study of photo-oxidation degradation mechanisms in P3HT for organic solar cells, *Phys. Chem. Chem. Phys* **16**, 8092 (2014).

[23] P. Musto, M. Abbate, M. Pannico, G. Scarinzi, and G. Ragosta, Improving the photo-oxidative stability of epoxy resins by use of functional poss additives: A spectroscopic, mechanical and morphological study, *Polymer* **53**, 5016 (2012).

[24] Y. Alexeev, M. Amsler, M. A. Barroca, S. Bassini, T. Battelle, D. Camps, D. Casanova, Y. J. Choi, F. T. Chong, C. Chung, *et al.*, Quantum-centric supercomputing for materials science: A perspective on challenges and future directions, *Fut. Gen. Comput. Sys* **160**, 666 (2024).

[25] K. Kanno, M. Kohda, R. Imai, S. Koh, K. Mitarai, W. Mizukami, and Y. O. Nakagawa, Quantum-selected configuration interaction: Classical diagonalization of Hamiltonians in subspaces selected by quantum computers, [arXiv:2302.11320](https://arxiv.org/abs/2302.11320) (2023).

[26] J. Robledo-Moreno, M. Motta, H. Haas, A. Javadi-Abhari, P. Jurcevic, W. Kirby, S. Martiel, K. Sharma, S. Sharma, T. Shirakawa, *et al.*, Chemistry beyond exact solutions on a quantum-centric supercomputer, [arXiv:2405.05068](https://arxiv.org/abs/2405.05068) (2024).

[27] D. Kaliakin, A. Shajan, J. R. Moreno, Z. Li, A. Mitra, M. Motta, C. Johnson, A. A. Saki, S. Das, I. Sittikov, *et al.*, Accurate quantum-centric simulations of supramolecular interactions, [arXiv:2410.09209](https://arxiv.org/abs/2410.09209) (2024).

[28] I. Liepuoniute, K. D. Doney, J. Robledo-Moreno, J. A. Job, W. S. Friend, and G. O. Jones, Quantum-centric study of methylene singlet and triplet states, [arXiv:2411.04827](https://arxiv.org/abs/2411.04827) (2024).

[29] S. Barison, J. R. Moreno, and M. Motta, Quantum-centric computation of molecular excited states with extended sample-based quantum diagonalization, *Quant. Sci. Tech* **10**, 025034 (2025).

[30] A. Eddins, M. Motta, T. P. Gujarati, S. Bravyi, A. Mezzacapo, C. Hadfield, and S. Sheldon, Doubling the size of quantum simulators by entanglement forging, *Phys. Rev. X Quantum* **3** (2022).

[31] M. Motta, W. Kirby, I. Liepuoniute, K. J. Sung, J. Cohn, A. Mezzacapo, K. Klymko, N. Nguyen, N. Yoshioka, and J. E. Rice, Subspace methods for electronic structure simulations on quantum computers, *Electron. Struct* **6**, 013001 (2024).

[32] W. J. Huggins, J. R. McClean, N. C. Rubin, Z. Jiang, N. Wiebe, K. B. Whaley, and R. Babbush, Efficient and noise resilient measurements for quantum chemistry on near-term quantum computers, *npj Quantum Inf* **7**, 23 (2021).

[33] S. Bravyi, G. Smith, and J. A. Smolin, Trading classical and quantum computational resources, *Phys. Rev. X* **6**, 021043 (2016).

[34] Q. Sun and G. K.-L. Chan, Quantum embedding theories, *Acc. Chem. Res* **49**, 2705 (2016).

[35] J. A. Smolin, J. M. Gambetta, and G. Smith, Efficient method for computing the maximum-likelihood quantum state from measurements with additive Gaussian noise, *Phys. Rev. Lett* **108**, 070502 (2012).

[36] I. Liepuoniute, M. Motta, T. Pellegrini, J. E. Rice, T. P. Gujarati, S. Gil, and G. O. Jones, Simulation of a Diels-Alder reaction on a quantum computer, *Phys. Chem. Chem. Phys* **26**, 25181 (2024).

[37] B. Bauer, S. Bravyi, M. Motta, and G. K.-L. Chan, Quantum algorithms for quantum chemistry and quantum materials science, *Chem. Rev* **120**, 12685 (2020).

[38] M. A. Castellanos, M. Motta, and J. E. Rice, Quantum computation of $\pi \rightarrow \pi^*$ and $n \rightarrow \pi^*$ excited states of aromatic heterocycles, *Mol. Phys* **122**, e2282736 (2024).

[39] H. F. Trotter, On the product of semi-groups of operators, *Proc. Am. Math. Soc* **10**, 545 (1959).

[40] J. Hubbard, Calculation of partition functions, *Phys. Rev. Lett* **3**, 77 (1959).

[41] R. L. Stratonovich, On a method of calculating quantum distribution functions, *Sov. Phys. Doklady* **2**, 416 (1957).

[42] S. Zhang and H. Krakauer, Quantum monte carlo method using phase-free random walks with slater determinants, *Phys. Rev. Lett* **90**, 136401 (2003).

[43] M. Motta and S. Zhang, Ab initio computations of molecular systems by the auxiliary-field quantum monte carlo method, *WIREs Comput. Mol. Sci* **8**, e1364 (2018).

[44] D. J. Thouless, Stability conditions and nuclear rotations in the hartree-fock theory, *Nuc. Phys* **21**, 225 (1960).

[45] R. Balian and E. Brezin, Nonunitary Bogoliubov transformations and extension of Wick's theorem, *Il Nuovo Cimento B* **64**, 37 (1969).

[46] B. Bremond, Hartree-Fock methods for degenerate cases, *Nuc. Phys* **58**, 687 (1964).

[47] H. Fukutome, Theory of resonating quantum fluctuations in a fermion system: resonating Hartree-Fock approximation, *Progr. Theor. Phys* **80**, 417 (1988).

[48] P. Å. Malmqvist, Calculation of transition density matrices by nonunitary orbital transformations, *Int. J. Quantum Chem* **30**, 479 (1986).

[49] A. J. Thom and M. Head-Gordon, Hartree-Fock solutions as a quasidiabatic basis for nonorthogonal configuration interaction, *J. Chem. Phys* **131**, 124113 (2009).

[50] E. J. Sundstrom and M. Head-Gordon, Non-orthogonal configuration interaction for the calculation of multielectron excited states, *J. Chem. Phys* **140**, 114103 (2014).

[51] M. Reck, A. Zeilinger, H. J. Bernstein, and P. Bertani, Experimental realization of any discrete unitary operator, *Phys. Rev. Lett* **73**, 58 (1994).

[52] W. R. Clements, P. C. Humphreys, B. J. Metcalf, W. S. Kolthammer, and I. A. Walmsley, Optimal design for universal multiport interferometers, *Optica* **3**, 1460 (2016).

[53] Z. Jiang, K. J. Sung, K. Kechedzhi, V. N. Smelyanskiy, and S. Boixo, Quantum algorithms to simulate many-body physics of correlated fermions, *Phys. Rev. Appl* **9**, 044036 (2018).

[54] The ffsim developers, *ffsim: Faster simulations of fermionic quantum circuits*.

[55] M. Motta, E. Ye, J. R. McClean, Z. Li, A. J. Minnich, R. Babbush, and G. K. Chan, Low rank representations for quantum simulation of electronic structure, *npj Quantum Inf* **7**, 1 (2021).

[56] Y. Matsuzawa and Y. Kurashige, Jastrow-type decomposition in quantum chemistry for low-depth quantum circuits, *J. Chem. Theory Comput* **16**, 944 (2020).

[57] M. Motta, K. J. Sung, K. B. Whaley, M. Head-Gordon, and J. Shee, Bridging physical intuition and hardware efficiency for correlated electronic states: the local unitary cluster Jastrow ansatz for electronic structure, *Chem. Sci* **14**, 11213 (2023).

[58] B. O'Gorman, W. J. Huggins, E. G. Rieffel, and K. B. Whaley, Generalized swap networks for near-term quantum computing, [arXiv:1905.05118](https://arxiv.org/abs/1905.05118) (2019).

[59] A. Rivaton, L. Moreau, and J.-L. Gardette, Photo-oxidation of phenoxy resins at long and short wavelengths—ii. mechanisms of formation of photoproducts, *Polym. Degrad. Stab* **58**, 333 (1997).

[60] E. Yousif and R. Haddad, Photodegradation and photostabilization of polymers, especially polystyrene, *SpringerPlus* **2**, 1 (2013).

[61] B. Mailhot, S. Morlat-Thérias, P.-O. Bussière, and J.-L. Gardette, Study of the degradation of an epoxy/amine resin, 2, *Macromolecular Chemistry and Physics* **206**, 585 (2005).

[62] 2,2-diphenylpropane (compound).

[63] A. D. Becke, Density-functional thermochemistry. III. the role of exact exchange, *J. Chem. Phys* **98**, 5648 (1993).

[64] S. Grimme, J. Antony, S. Ehrlich, and H. Krieg, A consistent and accurate ab initio parametrization of density functional dispersion correction (DFT-D) for the 94 elements H-Pu, *J. Chem. Phys* **132**, 154104 (2010).

[65] J. Dunning, Thom H., Gaussian basis sets for use in correlated molecular calculations. I. the atoms boron through neon and hydrogen, *J. Chem. Phys* **90**, 1007 (1989).

[66] Y. Cao, T. Balduf, M. D. Beachy, M. C. Bennett, A. D. Bochevarov, A. Chien, P. A. Dub, K. G. Dyall, J. W. Furness, M. D. Halls, T. F. Hughes, L. D. Jacobson, H. S. Kwak, D. S. Levine, D. T. Mainz, I. Moore, Kevin B., M. Svensson, P. E. Videla, M. A. Watson, and R. A. Friesner, Quantum chemical package Jaguar: a survey of recent developments and unique features, *J. Chem. Phys* **161**, 052502 (2024).

[67] G. Knizia, Intrinsic atomic orbitals: An unbiased bridge between quantum theory and chemical concepts, *Journal of Chemical Theory and Computation* **9**, 4834 (2013), pMID: 26583402, <https://doi.org/10.1021/ct400687b>.

[68] Q. Sun, T. C. Berkelbach, N. S. Blunt, G. H. Booth, S. Guo, Z. Li, J. Liu, J. D. McClain, E. R. Sayfutyarova, S. Sharma, *et al.*, PySCF: the Python-based simulations of chemistry framework, *WIREs Comput. Mol. Sci* **8**, e1340 (2018).

[69] Q. Sun, X. Zhang, S. Banerjee, P. Bao, M. Barbry, N. S. Blunt, N. A. Bogdanov, G. H. Booth, J. Chen, Z.-H. Cui, *et al.*, Recent developments in the PySCF program package, *J. Chem. Phys* **153**, 024109 (2020).

[70] S. Sharma, A. A. Holmes, G. Jeanmairet, A. Alavi, and C. J. Umrigar, Semistochastic heat-bath configuration interaction method: selected configuration interaction with semistochastic perturbation theory, *J. Chem. Theory Comput* **13**, 1595 (2017).

[71] H. Zhai, H. R. Larsson, S. Lee, Z.-H. Cui, T. Zhu, C. Sun, L. Peng, R. Peng, K. Liao, J. Tölle, *et al.*, Block2: a comprehensive open source framework to develop and apply state-of-the-art DMRG algorithms in electronic structure and beyond, *J. Chem. Phys* **159** (2023).

[72] C. Johnson, S. Barison, B. Fuller, J. R. Garrison, J. R. Glick, A. A. Saki, A. Mezzacapo, J. Robledo-Moreno, M. Rossmannek, P. Schweigert, I. Situdikov, and K. J. Sung, Qiskit addon: sample-based quantum diagonalization, <https://github.com/Qiskit/qiskit-addon-sqd> (2024).

[73] C. Piveteau and D. Sutter, Circuit knitting with classical communication, *IEEE Trans. Inf. Theor* **70**, 2734 (2023).

[74] B. Rånby, Photodegradation and photo-oxidation of synthetic polymers, *Journal of Analytical and Applied Pyrolysis* **15**, 237 (1989).

[75] B. Mailhot, S. Morlat-Thérias, M. Ouahioune, and J.-L. Gardette, Study of the degradation of an epoxy/amine resin, 1, *Macromolecular Chemistry and Physics* **206**, 575 (2005).

[76] A. Rivaton, L. Moreau, and J.-L. Gardette, Photo-oxidation of phenoxy resins at long and short wavelengths—i. identification of the photoproducts, *Polym. Degrad. Stab* **58**, 321 (1997).